FULL PAPER

Open Access

Derivation of 1.064 µm normal albedos on the C-type asteroid Ryugu from laser pulse intensity measurement of the Hayabusa2 LIDAR

Ryuhei Yamada[1*] , Keiko Yamamoto[2], Shoko Oshigami[3], Hiroshi Araki[2,9], Hiroki Senshu[4], Hirotomo Noda[5,9], Noriyuki Namiki[2,9], Koji Matsumoto[5,9], Fumi Yoshida[2,6], Shinsuke Abe[7], Naru Hirata[1], Sho Sasaki[8] and Takahide Mizuno[3]

Abstract

Japanese asteroid explorer Hayabusa2 arrived at C-type asteroid 162,173 Ryugu in June 2018. The laser altimeter (LIDAR) onboard Hayabusa2 measured its own transmitted laser and returned pulse intensities from a Ryugu surface until November 2019. Because the Ryugu surface is extremely rough, topography dominates over the material properties in the conventional derivation of normal albedo. Thus, we developed a method to retrieve the normal albedo from the rough surface of a C-type asteroid at a LIDAR laser wavelength of 1.064 µm. The albedo map covering an equatorial band between $-40°$ and $+20°$ in latitude was created with 3°-by-3° resolution using the intensity data obtained before the conjunction of the spacecraft with the Sun. The average of the normal albedo is 0.0405 ± 0.0027, whereas approximately half of the 3°-by-3° grids are between 0.04 and 0.045. The low and uniform normal albedo feature is common to other remote-sensing observations of Ryugu by visible and near-infrared cameras onboard Hayabusa2.

Keywords C-type asteroid, Albedo, LIDAR, Hayabusa2

Graphical Abstract
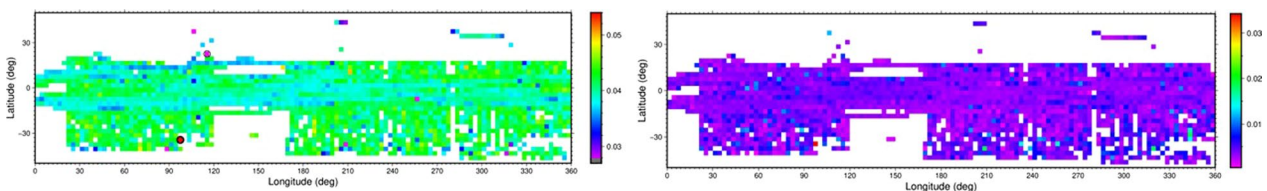
*Correspondence:
Ryuhei Yamada
ryamada@u-aizu.ac.jp
Full list of author information is available at the end of the article

Yamada *et al. Earth, Planets and Space*   (2022) 74:166

Page 2 of 18

Introduction

In June 2018, the Japanese asteroid explorer Hayabusa2 arrived at the C-type asteroid (162,173) Ryugu after cruising for about three and a half years. Ryugu is one of the near-Earth asteroids. Our knowledge of space weathering on a C-type asteroid surface, which contains carbon, organic matter, and water metamorphic minerals, is still limited. Hence, the survey of surface albedo distribution by Hayabusa2 is a unique opportunity to collect information on the space weathering of C-type asteroids. Besides space weathering, three mechanisms are considered causes of albedo variations on the asteroid surface: landslides due to tidal effects (Binzel et al. 2010), aqueous alteration (Vilas 2008; Sugita et al. 2013), and adherence of the material from other bodies (Reddy et al. 2012). Hayabusa2 has four scientific optical instruments: optical navigation camera (ONC), near-infrared spectrometer (NIRS3), thermal infrared imager (TIR), and laser altimeter (LIDAR). Sugita et al. (2019) conducted the first global albedo analysis of Ryugu using the ONC images. They reported that the asteroid had a relatively uniform surface reflectance. The geometric albedo was 0.045 ± 0.002 at 0.55 μm, similar to the darkest asteroids (235) Mathilde and other Cb-type asteroids (e.g., Bus and Binzel 2002). Ryugu's spectral feature between 0.4 and 0.9 μm is observed using ONC, indicating no 0.7 μm absorption band and little spectral variation. As a result of these properties, Ryugu is classified as a Cb-type overall, among the C-type. Nevertheless, boulders exhibit various color characteristics (Tatsumi et al. 2021). The global observation of Ryugu by NIRS3 also revealed a low reflectance of 0.017 ± 0.002 at 2.0 μm (Kitazato et al. 2019). Reflectance in visible (0.4–0.9 μm) and near-infrared (1.8–3.2 μm) regions indicates that Ryugu's surface is compositionally homogeneous and that the albedo is very low like a thermally and/or shock-metamorphosed carbonaceous chondrite (Sugita et al. 2019).

LIDAR surveys with a laser wavelength of 1.064 μm can fill the gap between the ONC and NIRS3 observations. In general, the spectral feature around 1.064 μm is an indicator of the olivine or pyroxene. These are the main components of planetary silicate materials, which enable the classification of target materials into meteorite types and the study of the surface evolution of asteroids. Therefore, the near-infrared spectrum around 1 μm was measured in the first Hayabusa mission and showed that the asteroid Itokawa was akin to ordinary chondrite (Kitazato et al. 2008). In addition, the albedo measurement of Itokawa by LIDAR was attempted during the first Hayabusa mission (Abe et al. 2006; Mukai et al. 2007). However, the results were inaccurate, because the former LIDAR could not simultaneously record the intensities of the transmitted and received pulses.

Hayabusa2 LIDAR records both the transmitted intensity and the corresponding returned pulse intensity for every laser shot. Hence, we can calculate, in principle, the albedo by comparing the transmitted and returned laser energy at 1.064 μm. LIDAR albedo measurement has three characteristics: (1) the active measurement, unlike other passive sensors, such as ONC or NIRS3, uses a well-calibrated light source; (2) albedo data are obtained at a zero-phase angle; and (3) the LIDAR measurement can fill the spectrum gap between ONC and NIRS3.

A key to the accurate derivation of the surface albedo is the precise energy estimation of the returned pulse, which is disturbed by the rough asteroid surface. As the received energy is an integration of the reflected pulse over time and space, detection and response by the LIDAR to the disturbed return are important for the estimation of albedo. For other planetary bodies, the albedo at 1.064 μm was measured using the Lunar Orbiter Laser Altimeter (LOLA) on the Moon (Smith et al. 2010) and the Mercury Laser Altimeter (MLA) on Mercury (Sun and Neumann 2015). They successfully identified albedo variations in the rough polar regions of the Moon and Mercury (e.g., Zuber et al. 2012; Neumann et al. 2013). The LOLA and MLA have multiple receiving telescopes, and the receiver can monitor the returned laser pulse energies and pulse widths above a threshold. These functions help estimate the shapes and energies of the returned pulses accurately.

The OSIRIS-REx Laser Altimeter (OLA) constructed the shape model of Bennu, another C-type asteroid similar to Ryugu, using laser ranging data (Seabrook et al. 2019; Barnouin et al. 2020; Daly et al. 2020). The preliminary albedo analysis was conducted using the return intensity count (Neumann et al. 2020). The OLA has two types of laser transmitters of different energies and can scan a field over 10° by 10° using a scanning mirror with a maximum sampling rate of 10 kHz (Daly et al. 2017; Barnouin et al. 2020). Nevertheless, the Hayabusa2 LIDAR only has NEAR and FAR receiving telescopes. One fixed laser transmitter obtains eight-bit digital values of the transmitted and received pulse energies with a maximum sampling rate of 1 Hz. Unlike other planetary laser altimeters, pulse shapes are not measured. Such hardware design is appropriate for small- and middle-class planetary explorations with limited resources. Therefore, this study's first objective is to establish a method to retrieve the normal albedo of the rough surface under the limitations of Hayabusa2 LIDAR. The second objective is to provide a map of the 1.064 μm albedo distribution on the C-type asteroid Ryugu.

The contents of this paper are as follows: "Pulse intensity measurement by the Hayabusa2 LIDAR" section reviews the specification and data acquisition of

Yamada *et al. Earth, Planets and Space* (2022) 74:166

Page 3 of 18

Hayabusa2 LIDAR. "Derivation of normal albedo for rough asteroid surfaces" section explains a method for deriving the normal albedo based on the return pulse simulation and the ground experimental results. In addition, the correction of periodic variation and the remaining errors in the normal albedo are discussed. Then, "Data selection" section describes the observation by the LIDAR on Ryugu and the data selection. "Results" section presents the results of the albedo mapping. Finally, we discuss the properties of the 1.064 μm albedo distribution, compare our results with those derived from ONC images in "Discussion" section, and conclude this study in "Conclusion" section.

Pulse intensity measurement by the Hayabusa2 LIDAR

Table 1 summarizes the specifications of Hayabusa2 LIDAR. See Mizuno et al. (2017) for further information, including the development processes. In this study, we analyzed only data taken by the "FAR" telescope, because the data taken by the "NEAR" telescope were not calibrated for the albedo measurement.

The laser pulses transmitted to the asteroid surface are recorded as eight-bit digital values. We call this record the transmitted pulse intensity (D_T), which can be converted to transmitted pulse energy E_T. The functional relationship between E_T and D_T has already been established by Yamada et al. (2017), and we improved it in "Re-evaluation of E_T from D_T" section.

A small fraction of the laser pulse reflected on the solid surface becomes an input to the LIDAR telescope, and power is detected by the internal avalanche photodiode (APD) [Fig. 3 in Yamada et al. (2017)]. The LIDAR

detection system sets three grades of APD responsivities: high, middle, and low, depending on the bias voltage applied to the APD (Table 1). The voltage output of the APD is processed in the integration and peak-hold circuits and is recorded as the received pulse intensity, D_R, which corresponds to the pulse energy received by the APD, E_{obs}. Yamada et al. (2017) describe the energy conversion from D_R to E_{obs} in a special case, where the return pulse is rectangular and 10-ns wide. In this paper, we generalize this conversion function to handle the variable-reflected waveforms expected for in situ observations.

Derivation of normal albedo for rough asteroid surfaces

Photometric model

Photometric models relating the incident irradiance, J, the scattered radiance, I, the bidirectional reflectance, the radiation factor, the disk function, $\xi(i, e)$, the phase function, $f(\alpha)$, and the normal albedo, ρ, are well described by Li et al. (2015) and are concisely summarized in Tables 1, 2, and 3. The relationship is expressed as

$$I(i, e, \alpha) = \frac{1}{\pi} \rho \frac{f(\alpha)}{f(0)} \xi(i, e) J, \tag{1}$$

where i, e, and α are the incident, emission, and phase angles, respectively. See relationships of symbols in Appendix: Table 5. For LIDAR observation, α is 0, and i equals e. Hence, Eq. (1) becomes

$$I(i, i, 0) = \frac{1}{\pi} \rho \xi(i, i) J. \tag{2}$$

Notably, Eq. (2) expresses a reflection within a beam divergence (Table 1) at the surface of Ryugu.

We need to relate I and J of Eq. (2) with the LIDAR measurements, E_{obs} and E_T. The laser pulse transmitted from LIDAR has both spatial and temporal intensity distributions. Thus, J is written as

Table 1 Specification of the Hayabusa2 LIDAR (Mizuno et al. 2017; Yamada et al. 2017)

Parameters	Values
Ranging range	30 m–25 km (NEAR system: below 1 km, FAR system: above 1 km)
Transmitted laser pulse energy	14.6 ± 1.1 mJ
Wavelength	1.064 μm
Half the bandwidth of laser pulse	5.6 ± 0.23 ns
The view angle of the FAR telescope	1.5 mrad
Full beam divergence of the transmitter	2.4 mrad
Area for laser receiving of the FAR telescope	0.0095 m^2
Transmissivity of the optical system	0.678
The responsivity of the APD for low level	50 ± 4.5 kV/W
The responsivity of the APD for middle level	166 ± 28 kV/W
The responsivity of the APD for high level	503 ± 83 kV/W
Maximum data sampling	1.0 Hz

Table 2 Widths and amplitudes of pulses synthesized for the LIDAR-EM experiment

Pulse shape	Peak amplitude	Full pulse width (ns)
Rectangular	60–240 (20 intervals)	50
	80–160 (40 intervals)	60–200 (20 ns intervals)
	200	60, 80
	240	60
Gaussian	80–200 (20 intervals)	20–200 (20-ns intervals)
Ascending	150, 200, 250	70–200 (10-ns intervals)
Descending	150	70–150 (10-ns intervals)
	200, 250	70–130, 150 (10-ns intervals)

Yamada *et al. Earth, Planets and Space* (2022) 74:166

Page 4 of 18

Table 3 Observation conditions in the selected 15 days

Date	Event	Altitude range (m)	Total of data
2018/7/20	Science observation at low altitude	6212–7832	36,827
2018/8/1	Science observation at middle altitude	5070–19,946	84,076
2018/8/6	Gravity measurement	828–20,641	85,625
2018/8/7	Gravity measurement	1416–10,296	41,291
2018/9/11	Touchdown rehearsal	1972–19,943	72,092
2018/9/20	MINERVA release	1531–19,788	76,794
2018/9/21	MINERVA release	54–15,235	32,620
2018/10/2	MASCOT release	647–19,624	84,798
2018/10/3	MASCOT release	46–2752	86,380
2018/10/4	MASCOT release	2670–14,406	47,039
2018/10/14	Touchdown rehearsal	6206–19,626	41,971
2018/10/15	Touchdown rehearsal	21–12,944	65,334
2018/10/24	Touchdown rehearsal	952–19,860	82,719
2018/10/30	Science observation at low altitude	5182–6735	33,787
2018/10/31	Science observation at low altitude	3134–5560	24,726

$$J_{xy} = E_{\mathrm{T}} \varepsilon_{xy} \tau \left(t - \frac{L_{xy}}{c} \right) \qquad (3)$$

where xy denotes the position within the beam divergence, and t is the time from the beginning of laser transmission. E_{T} is the energy injected into the beam divergence, which is equivalent to the transmitted energy of the laser pulse. ε_{xy} is the normalized beam pattern of the transmitted laser pulse and its integration within the beam divergence is unity (Fig. 1). The function $\tau(t)$ represents the normalized time-wise intensity profile of the transmitted laser beam (Fig. 2). The temporal integration

of $\tau(t)$ is unity. L_{xy} is the distance between xy and the LIDAR telescope, and c is the speed of light. The time delay of the laser reflection from the transmission is considered in τ of Eq. (3).

The scattered radiance at xy is given by substituting Eq. (3) with Eq. (2):

$$I_{xy}(i_{xy}, i_{xy}, 0) = \frac{E_{\mathrm{T}}}{\pi} \rho \xi_{xy}(i_{xy}, i_{xy}) \varepsilon_{xy} \tau \left(t - \frac{L_{xy}}{c} \right), \quad (4)$$

where i_{xy} is the incident angle at xy and is dependent on local topography. The received pulse energy input into the APD, E_{obs}, is calculated from the spatial and temporal
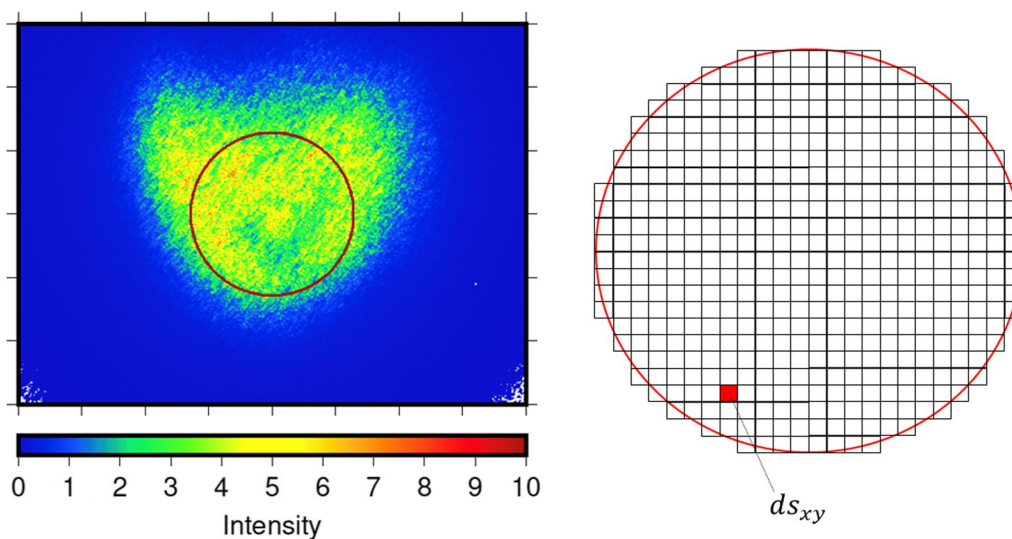

Fig. 1 Normalized transmitted laser beam pattern. The red circle on the left figure represents the field of view (FOV) of the FAR telescope. The right figure shows an image of numerical integration of the Ryugu surface within the FOV. See Eq. (5) for ds_{xy}
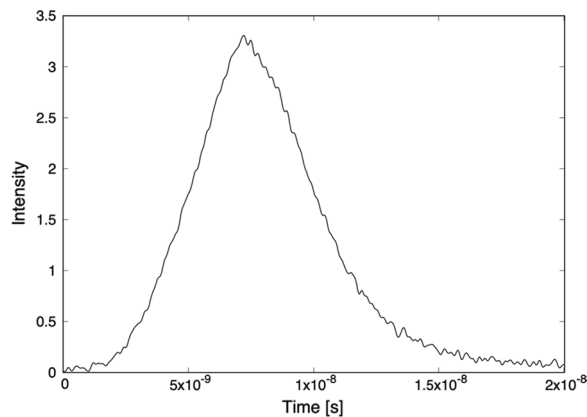
Yamada *et al. Earth, Planets and Space* (2022) 74:166

Page 5 of 18

Fig. 2 Example of a normalized transmitted laser waveform, $\tau(t)$. The vertical axis is arbitrary

Fig. 3 Schematic diagram of the experimental setup of the LIDAR-EM

integration of Eq. (4) by considering energy transfer from the asteroid surface to the APD:

$$E_{\mathrm{obs}} = \frac{E_{\mathrm{T}}}{\pi} \rho\beta \int dt \int_{\mathrm{footprint}} ds_{xy} \xi_{xy}\left(i_{xy}, i_{xy}\right) \varepsilon_{xy} \frac{A_0}{L_{xy}{}^2} \tau\left(t - \frac{2L_{xy}}{c}\right),$$

(5)

where β is the transmissivity of the optical system of the receiver (Table 1). The laser footprint considered in the above spatial integration corresponds to the field of view (FOV) of the receiving telescope, because the FOV is narrower than the full beam divergence of the transmitter (Table 1); ds_{xy} is the small area within the footprint (Fig. 1). A_0 is the aperture area of the receiving FAR telescope, 0.0095 m^2 (Table 1), and $A_0/L_{xy}{}^2$ is the solid angle of the aperture viewed from xy. Moreover, the time delay of laser reception from reflection is considered.

The estimation of E_{obs} is explained in the next section. The calculation of Eq. (5) requires waveform simulation. The numerical procedures of the simulation are described in detail in "Waveform simulation using a shape model" section.

Estimation of E_{obs} from D_{R}

To estimate E_{obs} from D_{R}, we need to know the response of the signal processing unit of LIDAR to various return pulse waveforms. Thus, we conducted an experiment using the LIDAR-Engineering Model (EM). The experiment comprises three steps: (1) synthesizing return pulses whose waveforms are either rectangular, Gaussian, or triangular; (2) inputting these laser pulses into the LIDAR-EM and recording D_{R} for each pulse; and (3) simultaneously measuring the strength of the laser pulse as a voltage signal using an oscilloscope and integrating over time. The integrated voltage, S_{v}, is proportional to E_{obs}. Furthermore, we determined the ratio of S_{v} and E_{obs} using the data taken in a thermal vacuum experiment.

LIDAR-EM experiment

The LIDAR-EM was manufactured to examine the function of the LIDAR flight model even after the launch of Hayabusa2. The laser pulses were synthesized using a laser pulse generator developed at the Chiba Institute of Technology (Senshu et al. 2017), which can control the laser pulse's time width and peak amplitude from 10 to 2000 ns every 10-ns step and 256 levels (0–255), respectively. The time profile of the synthesized laser pulse was detected using the PIN photodiode in the generator and recorded as the voltage signal using an oscilloscope. The oscilloscope's sampling rate is 10^9 Hz at its highest. S_{v} can be calculated from this record. Figure 3 shows a schematic diagram of the experimental setup. The designed laser pulse was transmitted into the FAR telescope of the LIDAR-EM, and the LIDAR-EM itself recorded D_{R} with a 1 Hz sampling rate. The recorded D_{R} was sent to the Ground Support Equipment (GSE) as telemetry data. In this experiment, all data were measured using APD low responsivity (Table 1).

We examined four types of input laser pulses. First, the rectangular pulse is tested for two purposes: to determine the relationship between E_{obs} and S_{v} by comparison with a preflight test and to determine the maximum pulse width that the signal processing unit can handle. We varied the input pulse width and amplitude (Table 2). Second, Gaussian-shaped waveforms are tested as a realistic return pulse from the rough and undulated surface of Ryugu. We similarly varied the full width and peak amplitude of Gaussian pulses (Table 2). Third and fourth, triangular-shaped waveforms whose amplitudes increase or decrease with time are tested. For those ascending and descending pulses, three peak amplitude levels were set with variable full widths (Table 2). For all combinations of amplitude and width, we measured approximately 60 pairs of D_{R} and S_{v}. Figure 4 shows examples of the four types of pulse shapes recorded in the oscilloscope.

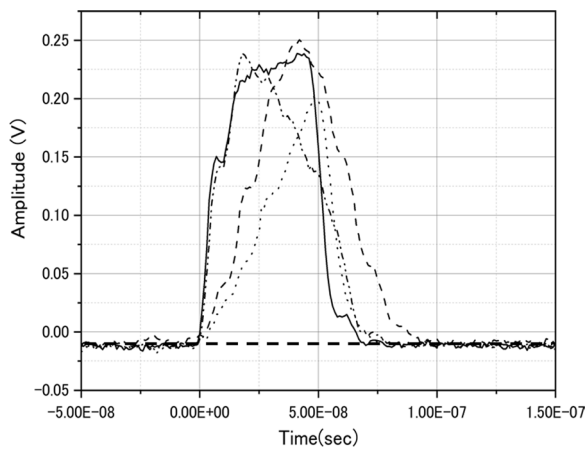Yamada *et al. Earth, Planets and Space* (2022) 74:166

Page 6 of 18

Fig. 4 Examples of four types of input laser pulses in the LIDAR-EM experiment. Solid, dashed, dotted, and dash–dotted lines indicate rectangular, gaussian, ascending triangular, and descending triangular pulses, respectively. Widths and peak amplitudes are 60 ns and 120, 40 ns and 120, 70 ns and 150, and 70 ns and 150, respectively. The horizontal thick dashed line indicates the noise floor of the records

Experimental results

We estimated the maximum pulse width that the LIDAR receiver could handle using rectangular pulses. Figure 5 shows the relationship between the pulse width and D_R for the rectangular pulses. This figure indicates that the D_R reaches an upper limit when the pulse width is longer than 90 ns (vertical dashed line in Fig. 5). This upper limit probably occurs, because the input laser pulse longer than 90 ns is truncated in the signal processing unit of the LIDAR.

Figure 6 shows the relationships between D_R and S_v for the four types of input pulses. Figure 6a shows the relationship using 3089 measurements, excluding the
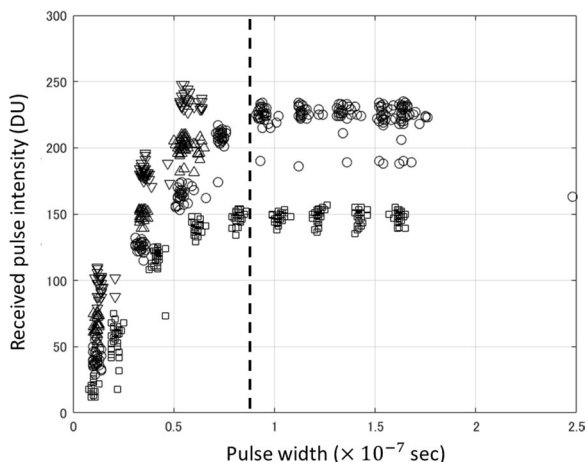

Fig. 5 Pulse width and D_R for the rectangular pulses. Different symbols denote peak amplitudes of 80, 120, 150 and 180 (Table 2). The dashed vertical line indicates the 90 ns limit

saturated data ($D_R = 255$) and signals too low to be distinguished from noise ($D_R \leq 10$). Figure 6b shows 1639 data whose width is shorter than 90 ns. The widths of the Gaussian and triangular pulses are measured for the range, where the amplitude exceeds the noise floor (Fig. 4). Regardless of the pulse shape, we found a clear relationship between D_R and S_v for pulses shorter than 90 ns.

Furthermore, we translated S_v of Fig. 6b into E_{obs}. Nevertheless, the relationship of D_R, S_v, and E_{obs} is determined for only 10-ns rectangular pulses in the pre-flight test (Yamada et al. 2017). Hence, we derive a constant proportionality between S_v and E_{obs} from 10-ns
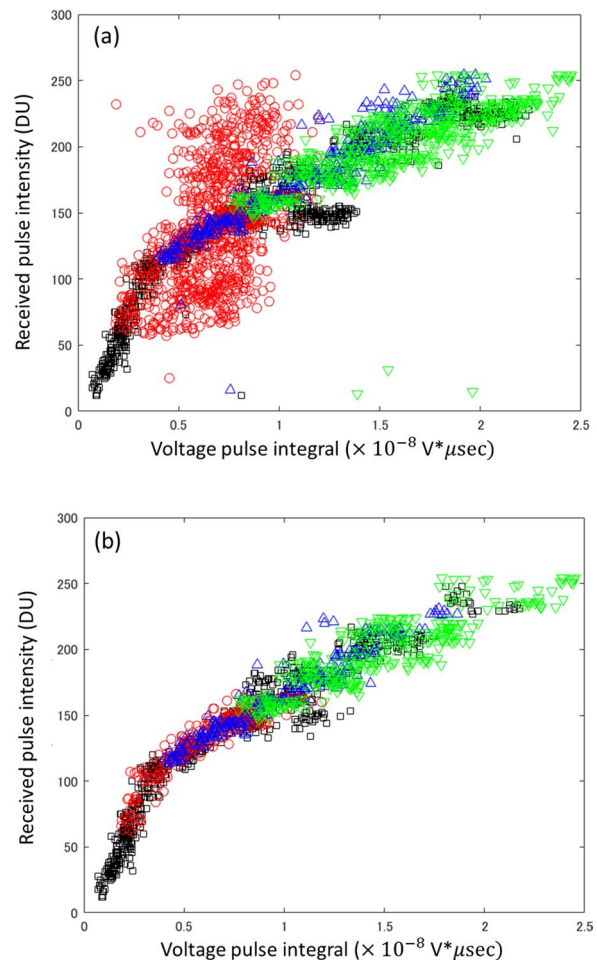

Fig. 6 D_R and S_v: **a** all measured pulses excluding $D_R = 255$ or ≤ 10, **b** pulses shorter than 90 ns. Black rectangles, red circles, blue upward triangles, and green downward triangles represent rectangular, gaussian, ascending triangular, and descending triangular pulses, respectively. The non-linear relation between the voltage pulse integral and received pulse intensity is likely due to the characteristics of the integration and peak-hold circuits of the receiver

Yamada *et al. Earth, Planets and Space* (2022) 74:166

Page 7 of 18

rectangular pulses and apply it to all other data shown in Fig. 6b.

Yamada et al. (2017) show a relationship between E_{obs} and D_R of specifically 10-ns rectangular pulses, namely, E_{obs}^{rec} and D_R^{rec}, as

$$E_{obs}^{rec}(D_R^{rec}) = \frac{R_s(D_R^{rec})\sigma_R}{G}, \tag{6}$$

where G is the responsivity of the APD and was set as the low level in the test (Table 1). σ_R is the pulse width (10 ns), and $R_S(D_R^{rec})$ is the conversion function from D_R^{rec} to the output peak voltage of the APD:

$$R_S(D_R^{rec}) = -6.79 \times 10^{-11} D_R^{rec4}$$
$$+ 1.10 \times 10^{-7} D_R^{rec3} - 5.40$$
$$\times 10^{-6} D_R^{rec2} + 1.36$$
$$\times 10^{-3} D_R^{rec} + 2.92 \times 10^{-2} \tag{7}$$

(Yamada et al. 2017). In the LIDAR-EM experiment, 35 pairs of D_R^{rec} and S_v^{rec} are taken for a 10-ns rectangular pulse. The relationship between S_v^{rec} and E_{obs}^{rec} is derived by substituting these D_R^{rec} into Eqs. (6) and (7) (Fig. 7). We estimated the error of E_{obs}^{rec} in "Error of E_{obs}" section. Using such an error as a weight, the constant proportionality of S_v^{rec} and E_{obs}^{rec} is derived. Applying this proportionality to all four types of waveforms,

$$E_{obs} = 1.09 \times 10^{-6} S_v, \tag{8}$$

is obtained. Figure 8 is drawn from Fig. 6b. E_{obs} in Fig. 8 can be fitted by a fifth polynomial equation (red line) as:
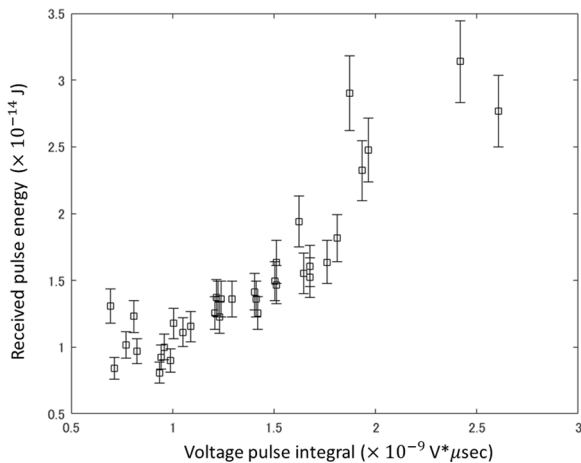

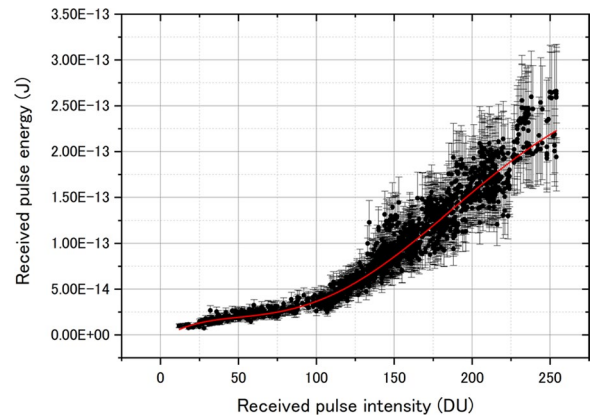**Fig. 8** E_{obs} and D_R. The fifth polynomial equation is fitted to the data (red line)

$$E_{obs}(D_R) = 8.38 \times 10^{-25} D_R^5 - 7.45$$
$$\times 10^{-22} D_R^4 + 2.23$$
$$\times 10^{-19} D_R^3 - 2.34$$
$$\times 10^{-17} D_R^2 + 1.19$$
$$\times 10^{-15} D_R - 5.40 \times 10^{-15} \tag{9}$$

Equation (9) is given for the low responsivity of the APD. The right-hand side of this equation should be amplified by the responsivity ratios in Table 1 for middle and high APD responsivities.

Waveform simulation using a shape model

Let us define a function, $\varphi_{eff}(t)$, by taking a spatial integration of Eq. (5).

$$\varphi_{eff}(t) = \int_{footprint} ds_{xy}\xi_{xy}(i_{xy}, i_{xy})\varepsilon_{xy}\frac{A_0}{L_{xy}^2}\tau\left(t - \frac{2L_{xy}}{c}\right), \tag{10}$$

$\varphi_{eff}(t)$ is the efficiency of energy reflection within a footprint. If the asteroid surface is flat, φ_{eff} can be simply calculated using nearly constant i_{xy}, ξ_{xy}, and L_{xy}. However, on the very rough surface of Ryugu, the laser beam emitted from the LIDAR transmitter was reflected and scattered on the undulating surface. The surface undulations within the footprint disturb the waveform of the return pulse. We need to eliminate such a topographic effect to study the composition of surface materials from albedo. Therefore, we include waveform simulation in the following calculation of φ_{eff}.

The second purpose of the waveform simulation is to exclude return pulses longer than 90 ns from our analysis, as discussed in the previous section. As Hayabusa2 LIDAR lacks a function for measuring the return pulse; instead, we estimated the return pulse's temporal profile

Fig. 7 S_v^{rec} and E_{obs}^{rec} for the 35 short rectangular pulses whose width is 10 ns

Yamada *et al. Earth, Planets and Space* (2022) 74:166

Page 8 of 18

from Eq. (10). Strictly, $\tau(t)$ differs for every laser shot. However, without onboard measurements of $\tau(t)$, we adopted the representative transmitted waveform derived from the thermal vacuum test (Fig. 2).

We used a shape model developed from the images taken by the ONC to simulate Ryugu topography (Watanabe et al. 2019). The laser footprint was divided into small area elements for numerical integration (Fig. 1). The return pulse waveform from each element is calculated considering ε_{xy}, L_{xy}, and ξ_{xy}. Finally, the return pulse waveform is calculated by numerically integrating the returns from all elements in the footprint.

For numerical integration of Eq. (10), we applied two types of reflection laws, namely, Lambert and Lommel–Seeliger (Jantunen and Raitala 1983; Shkuratov et al. 2011; Li et al. 2015), and compared the results (see "Results" section). They are given as follows:

$$\xi_{xy} = cos\theta_{xy} (\text{Lambert law}),$$

$$\xi_{xy} = 1 (\text{Lommel} - \text{Seeliger law}), \tag{11}$$

where θ_{xy} is the average incident angle in the laser footprint. Notably, there are two definitions of Lommel–Seeliger law (Shkuratov et al. 2011; Li et al. 2015), which differ by a factor of 2. We used Eq. (13) by Shkuratov et al. (2011) for the consistency of the calculated normal albedo.

Besides the Lambert and Lommel–Seeliger laws, Yokota et al. (2022) applied three other reflection laws and found no difference in albedo for all five laws. The Oren–Nayar model is another reflectance law often used for rough planetary surfaces (Oren and Nayar 1994). However, this law requires a roughness parameter, which is difficult to estimate for each footprint. Thus, we use only two laws in Eq. (11).

ε_{xy} in Eq. (5) is not spatially uniform and varies for each laser transmission. We averaged 1200 different beam patterns obtained in the thermal vacuum test and normalized them (Fig. 1). The uncertainty of the ε_{xy} will be discussed in "Errors of E_T and ϕ_{eff}" section. As described above, only part of the beam is inside the FOV of the receiving telescope (Fig. 1) and is used for Eq. (10).

The L_{xy} and θ_{xy} in Eqs. (5) and (11) depend on the topographic undulations of Ryugu. These values are obtained from a shape model of Ryugu developed from ONC images (SHAPE_SPC_3M_v20200323, an updated version of Watanabe et al. 2019), which comprises of 3,145,728 facets and 1,579,014 vertices. We

divided the FOV with a diameter of 1.44 mrad into elements of $(5.58 \times 10^{-3})^2$ mrad^2 (the right side of Fig. 1). The area of ds_{xy} is in the range between 0.0025 to 0.000031 m^2 depending on the altitude between 1 and 9 km. Therefore, ds_{xy} is small compared with the average area of the facets of the shape model of 0.89 m^2. We consider that ds_{xy} does not span multiple facets of the shape model. The L_{xy} and θ_{xy} are calculated from xy to the spacecraft position estimated by Matsumoto et al. (2020).

The value of L_{xy} differs for each ds_{xy} owing to the surface topography of Ryugu. Consequently, the laser reflection time at the surface and the reception time at the LIDAR telescope also differ for each ds_{xy}. This delay of time appears in Eq. (5) as $\tau(t - 2L_{xy}/c)$. dt in Eq. (5) is set as 2.5×10^{-11} s for numerical integration, which corresponds to 0.0075 m at the speed of light and is small enough for the 90 ns criteria of the return pulse.

Figure 9 shows examples of the calculated waveform of the return pulses and the topography of the Ryugu shape model within the laser footprints. The topography in the right example is more undulated than that in the left one. Thus, in the right example, the waveform deviates from the transmitted pulse shown in Fig. 2, whereas the left examples are similar to the Gaussian form. The blue dotted line in Fig. 9 indicates the average calculated return pulse for the 25,964 observations on October 30, 2018. Notably, the amplitude of the return pulse is smaller in the right example than in the left, because the observation altitude differs.

Re-evaluation of E_T from D_T

The conversion function from D_T to E_T has been determined by a thermal vacuum test conducted before the Hayabusa2 launch. Figure 10 shows the measurements of E_T and D_T. The straight blue line is derived by fitting a linear equation in our previous study (Yamada et al. 2017). We adopted the third polynomial equation in this study to better fit the experimental results (the black solid curve in Fig. 10):

$$E_T(D_T) = -6.04 \times 10^{-7} D_T^3 + 2.36 \times 10^{-4} D_T^2 - 3.05 \times 10^{-2} D_T + 1.32. \tag{12}$$

In the thermal vacuum test, we have measured D_T ranging from 115 to 136. In principle, E_T increases with D_T. However, for the D_T smaller than 117, the experiment results show that E_T decreases as D_T increases (Fig. 10). Such behavior is unreasonable; hence, we exclude the results of D_T below 117 in the derivation of Eq. (12). Accordingly, we excluded data sets whose D_T is lower than 117, as described in "Data selection" section.

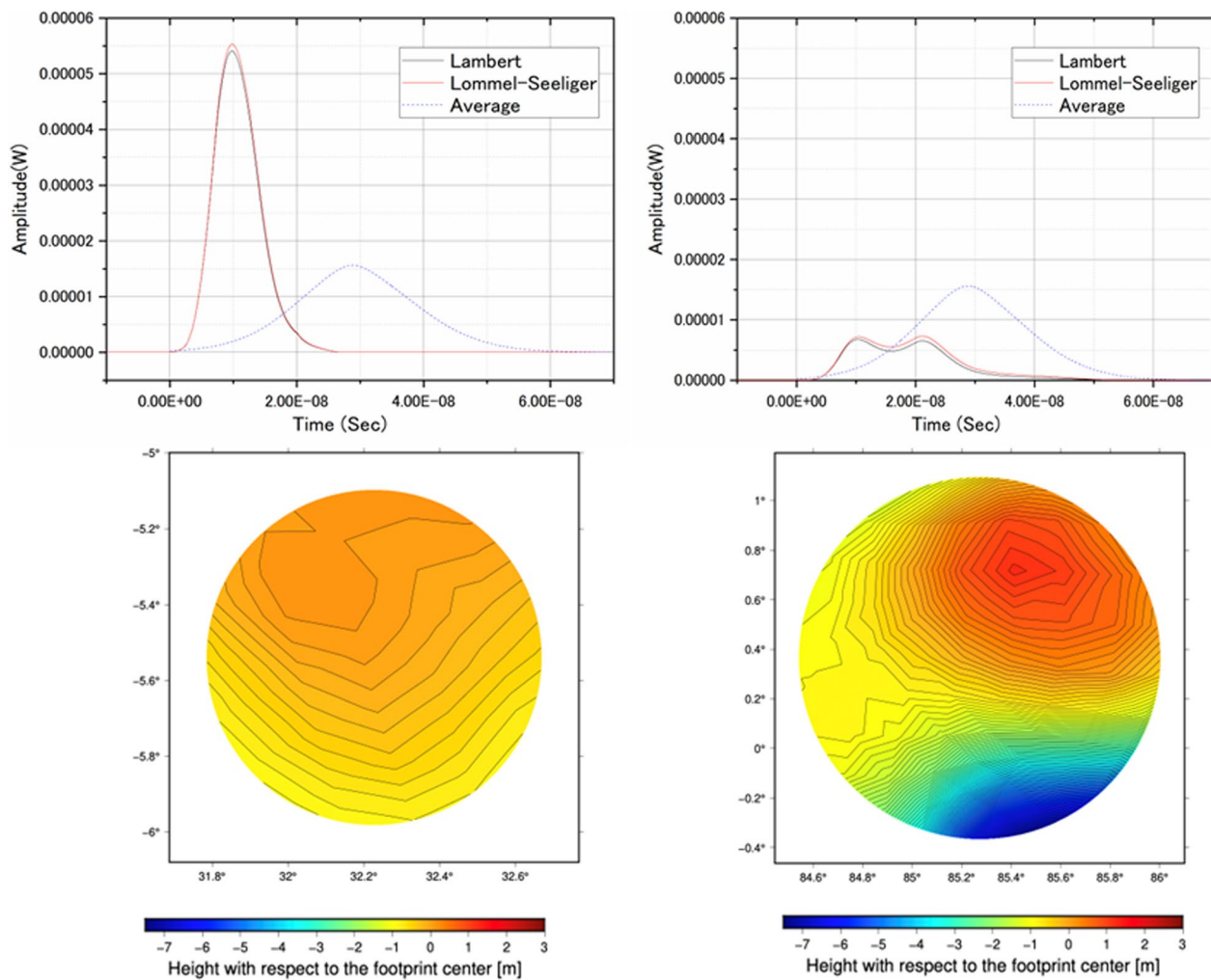Yamada *et al. Earth, Planets and Space* (2022) 74:166

Page 9 of 18

Fig. 9 Examples of the calculated return pulse waveforms and the corresponding footprint topographies derived from the Ryugu shape model. (Left) The transmitted time is 17:33:56 on 1 August 2018. The transmitted energy is 0.00151 J. Distance between the spacecraft and the footprint center is 5155 m. The mean incident angle in the footprint is 0.204 rad. (Right) The transmitted time is 8:44:06 on 1 August 2018. The transmitted energy is 0.00133 J. Distance between the spacecraft and the footprint center is 8589 m. The mean incident angle in the footprint is 0.464 rad. The blue dotted line shows the average of 25,964 return pulses taken on 3-October 2018

Calculation and correction of normal albedo

Equation (12) does not depend on temperature; however, LIDAR heater cycles influence in-situ observational data. The upper panel of Fig. 11a represents a time series albedo calculated from the data acquired on July 20, 2018, as an example. There is an obvious periodic variation in the albedo with a frequency of approximately 400 s. A periodic variation with the same frequency is also seen in the time series transmitted energy (Fig. 11b, upper panel).

These periodic variations are synchronized with the heater cycle. Figure 11b (bottom panel) shows the time series temperature of the transmitter's laser diode. Hence, the periodic variation is artificial; thus, we eliminated

these frequency components. Because the heater cycle depends on the thermal condition of the LIDAR, the frequency components from 0.002 to 0.0032 Hz are removed from the calculated albedo using low and high-pass filters. The bottom panel of Fig. 11a shows the corrected albedo after removing the periodic components.

Error of albedo derivation

From Eqs. (5) and (10), an error of normal albedo, $\delta\rho$, can be evaluated by the following equation:

$$\frac{\delta\rho}{\rho} = \sqrt{\left(\frac{\delta E_{\text{obs}}}{E_{\text{obs}}}\right)^2 + \left(\frac{\delta E_{\text{T}}}{E_{\text{T}}}\right)^2 + \left(\frac{\delta\varphi_{\text{eff}}}{\varphi_{\text{eff}}}\right)^2}, \quad (13)$$

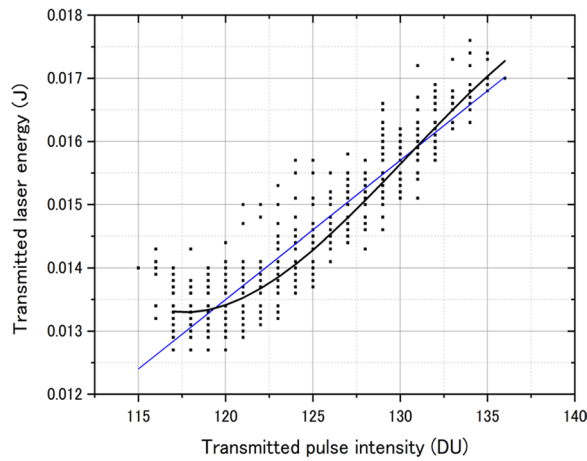Yamada *et al. Earth, Planets and Space* (2022) 74:166

Page 10 of 18

Fig. 10 E_T and D_T. The third polynomial equation is adopted as the conversion function of the transmitted energy (thick black line). The straight blue line is previously derived by Yamada et al. (2017)

where δE_{obs}, δE_T, and $\delta\varphi_{eff}$ are errors of E_{obs}, E_T, and φ_{eff}, respectively.

Error of E_{obs}

δE_{obs} is derived from Fig. 8, whereas the error of each point in Fig. 8 is evaluated from Fig. 7. Conversely, errors in the points in Fig. 7, δE_{obs}^{rec}, is derived from Eq. (6):

$$\frac{\delta E_{obs}^{rec}}{E_{obs}^{rec}} = \sqrt{\left(\frac{\delta G}{G}\right)^2 + \left(\frac{\delta R_S\left(D_{obs}^{rec}\right)}{R_S\left(D_{obs}^{rec}\right)}\right)^2}, \quad (14)$$

where δG is the error of responsivity of the APD in low gain and is 9.0% (Table 1). $\delta R_S(D_{obs}^{rec})$ is the fitting error of $R_s(D_{obs}^{rec})$ in Eq. (7) in low gain and is 3.7% (Yamada et al. 2017). Then, $\delta E_{obs}^{rec}/E_{obs}^{rec}$ is 9.7%. The digitization noise of D_R is automatically included in Fig. 6b. Thus, this error is considered at the 9.7% value.

All points in Fig. 7 are attached with 9.7% error bars. Then, the ratio of E_{obs} and S_v is calculated with this weight. Consequently, the standard deviation of this fitting is evaluated as much as 19.2%. Using this 19.2% error as a weight, Eq. (9) is derived. Then, $\delta E_{obs}/E_{obs}$ becomes 15.3%.

Errors of E_T and φ_{eff}

In Eq. (5), the error of β is excluded, because it has been precisely measured, as shown in Table 1. δE_T is calculated as the fitting error of Eq. (12). Using 1802 data sets included in Fig. 10, $\delta E_T/E_T$ of 1.78% is derived. Figure 10 includes the digitization noise of D_T and so does the 1.78% value.

φ_{eff} in Eq. (10) includes three variables: ξ_{xy}, L_{xy} and ε_{xy}. ds_{xy} is the function of L_{xy} ("Waveform simulation using a shape model" section). For the Lommel–Seeliger law, which we prefer to the Lambert model as described later, ξ_{xy} is a constant [Eq. (11)]. Since it is difficult to calculate these three errors directly, we calculated φ_{eff} values by changing ε_{xy}, $\tau(t)$ and L_{xy} independently within possible ranges.

We calculated φ_{eff} using 1200 different beam patterns for one specific location and obtained a deviation of 2.4% to investigate a error due to dispersion of ε_{xy}. In addition, we repeated the same evaluations for several other locations measured in different terrains and obtained similar results.

Similarly, for $\tau(t)$, we calculated φ_{eff} using intensity profiles of 1200 measurements in the thermal vacuum test for several locations. Then, the deviation of φ_{eff} is evaluated to be less than 0.5%.

For the error of L_{xy}, both uncertainties of the spacecraft orbit and the shape model require consideration. According to Yamamoto et al. (2020), the errors of the spacecraft orbit (Matsumoto et al. 2020) are 1.95 m in the direction of the transmitted laser. Watanabe et al. (2019) compared the heights of some boulders in a shape model constructed by the SPC (stereo photo clinometry) method with LIDAR's laser ranging data. They found that the shape model had an uncertainty of approximately 2 m. Therefore, we considered 2.79 m as the error of L_{xy} from a root of the mean square of the orbital and shape model errors. Similar to ε_{xy} and $\tau(t)$, φ_{eff} are also calculated by changing L_{xy} within range of ± 2.79 m at the lowest and highest altitudes, namely, 1066 and 9000 m. The variations of Eq. (5) for the highest and lowest altitudes are 0.52% and 0.062%, respectively.

In the above argument, we considered the L_{xy} error only in the line of sight. However, the spacecraft orbit and shape models also have errors in a horizontal direction. These errors result in uncertainty regarding the location of the laser footprint. We evaluated this uncertainty as a deviation of albedo values within a 3°-by-3° grid and discussed it in "Albedo map around the equator" section.

In total, $\delta\varphi_{eff}/\varphi_{eff}$ is derived as 2.5% from the RMS errors of ε_{xy}, $\tau(t)$ and L_{xy}. Consequently, the uncertainty of Eq. (5) is evaluated as 3.1%. Finally, $\delta\rho/\rho$ of 15.6% was derived from Eq. (13) using an uncertainty of Eq. (5) of 3.1% and $\delta E_{obs}/E_{obs}$ of 15.3%.

Data selection

The LIDAR observation of Ryugu started on June 26, 2018, and finished on November 14, 2019. D_T and D_R were continuously obtained at a sampling rate of 1/32 Hz at the home position of the spacecraft, namely, at an altitude of approximately 20 km around
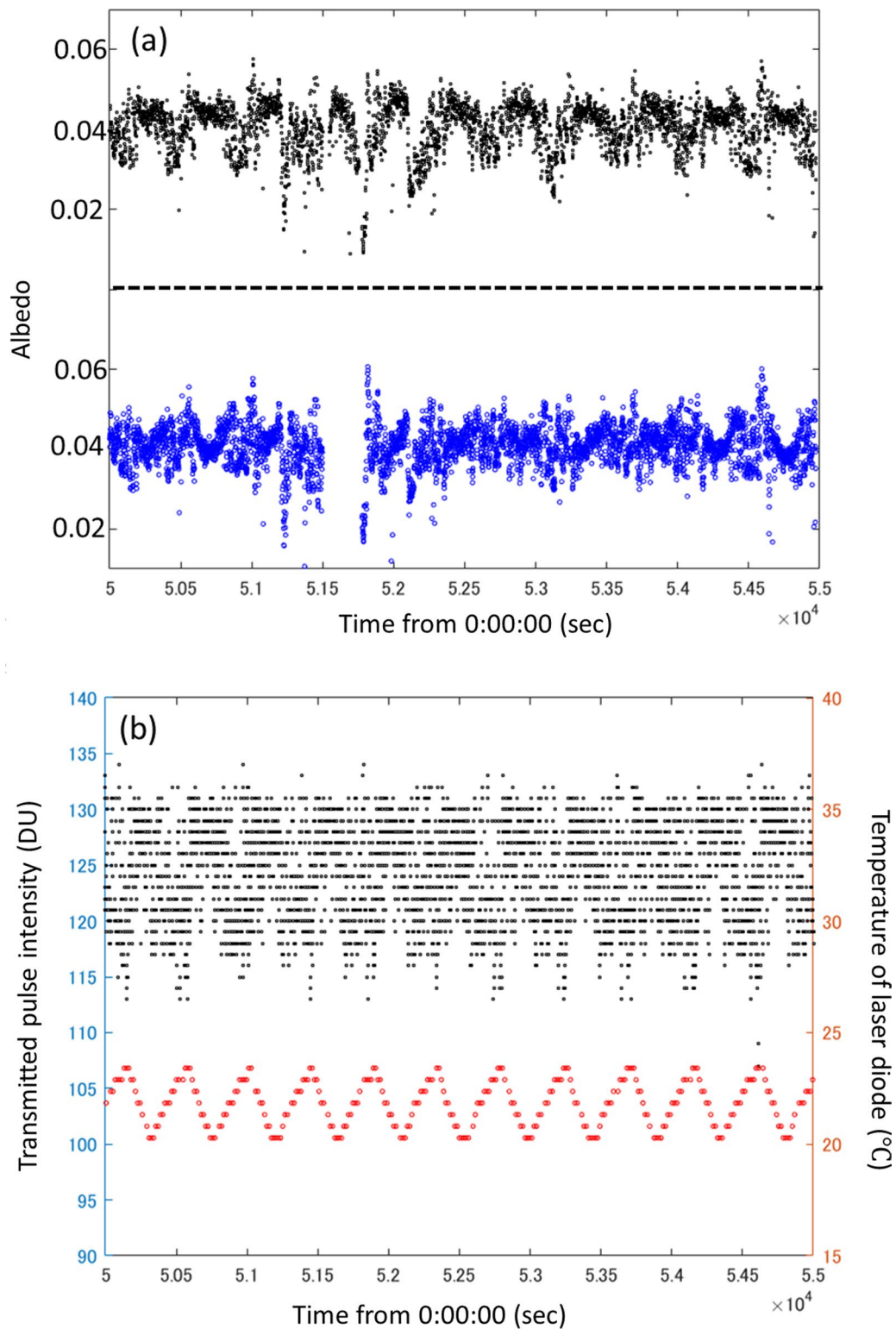
Yamada *et al. Earth, Planets and Space* (2022) 74:166

Page 11 of 18

Fig. 11 a Time variation of the albedo derived from the LIDAR data: uncorrected albedo in the top panel and corrected albedo in the bottom panel. **b** Time variation of the transmitted pulse intensity (black points) and the temperature of the laser diode of the transmitter (red points). The data were taken on 20 July 2018

Yamada *et al. Earth, Planets and Space* (2022) 74:166

Page 12 of 18

the equator of Ryugu (Watanabe et al. 2019). However, D_R obtained at the home position are between 5 and 20 DU, which are too low to estimate normal albedo considering the measurement errors described in "Error of albedo derivation" section. However, in some special operations, such as touchdown and gravity measurement, the spacecraft descended from the home position to an altitude below 10 km, acquiring D_T and D_R at a rate of 1 Hz. We used only data taken at altitudes lower than 9 km by the FAR telescope. Using this criterion, D_R are constrained between 100 and 200 DU, and a sufficiently high S/N is secured.

The LIDAR's FAR telescope was likely contaminated by surface regolith flown by the first touchdown in February 2019. Therefore, we further limited the data to those obtained before a conjunction that continued from the end of November to the end of December 2018. Low- and middle-altitude operations were conducted for 15 days before the conjunction (Table 3). These observations cover only the areas around the equator, where special operations were conducted.

As described in "Estimation of E_{obs} from D_R" section, D_R whose widths exceeds 90 ns are eliminated from our analysis. This limit corresponds to 30 m in either height difference within a footprint or footprint elongation. For example, if the spacecraft points at its nadir, the largest footprint size is 11 m for an altitude below 9 km. Therefore, the 90 ns limit is applied only when a footprint crosses the side of the boulder larger than 30 m. In addition, we removed D_R more than 250 to avoid saturation and D_T less than 117, as described in "Re-evaluation of E_T from D_T" section. Finally, we obtained the 390,456 sets of D_T and D_R, that is approximately 44% of the total observation data.

Results
Reflectance laws of Ryugu
First, we evaluated Lambert and Lommel–See liger's reflection laws. These laws have different dependencies on the incident angle [Eq. (11)]. We plotted normal albedos calculated based on these two laws for the average incident angle in the footprint (Fig. 12). The albedo values systematically increased with an incident angle for the Lambert law (blue dots). Conversely, for the Lommel–Seeliger law (red dots), the values are randomly distributed around an average regardless of the incident angle.

If the reflectance law [Eq. (11)] is suitably included, ρ should be independent of the incident angle. Thus,

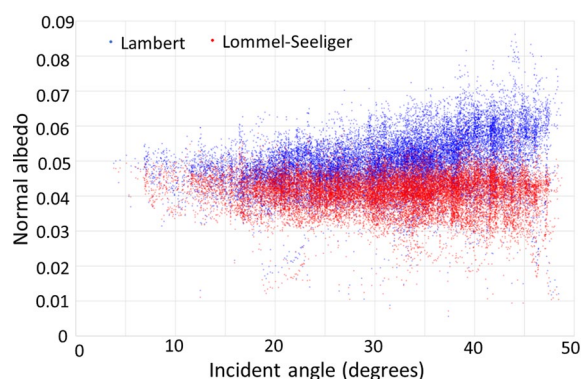**Fig. 12** ρ and incident angle for the two reflectance laws; the Lambert (blue) and the Lommel–Seeliger (red). The 31,647 data are shown for each law. These data were obtained on 20 July 2018 (Table 3) and were selected following the procedures described in Chapter 4. In this selection, the data for incident angles higher than 50° were excluded, because the widths of D_R are longer than 90 ns (See Estimation of E_{obs} from D_R)

we concluded that the Lommel–Seeliger law is preferable to the Lambert law for Ryugu. The difference arises from the application of Eqs. (5) and (10) to E_{obs} values, which are generally not dependent on the incident angle. These results agree with the photometric characteristics of Ryugu obtained from ground-based observations (Li et al. 2015; Le Corre et al. 2018). We adopted the Lommel–Seeliger law [the lower part of Eq. (11)] in the calculation.

Albedo map around the equator
Figure 13 shows all the calculated normal albedo values for each footprint after correcting periodic variation. We average albedos within a square grid pf 3°-by-3°, because neighboring footprints overlap depending on their sizes. The length of 1° in latitude on Ryugu is 7.5 m, assuming a sphere. However, the spacecraft position is estimated by comparing the profile of the laser ranges with the topographic cross section of the shape model along a track (Matsumoto et al. 2020). The uncertainty of the spacecraft's position also increases with altitude, because the size of the laser footprint increases with the altitude of the spacecraft. Yamamoto et al. (2020) evaluated this uncertainty as twice the footprint-22.5 m on the Ryugu surface from a 9 km altitude. Therefore, each 3°-by-3° grid can cover the uncertainty of the laser footprint at an altitude lower than 9 km. Furthermore, we counted the number of footprints whose centers are located in the grid for each 3°-by-3° grid and mapped those numbers in Fig. 14. The largest number is 1080. This grid is
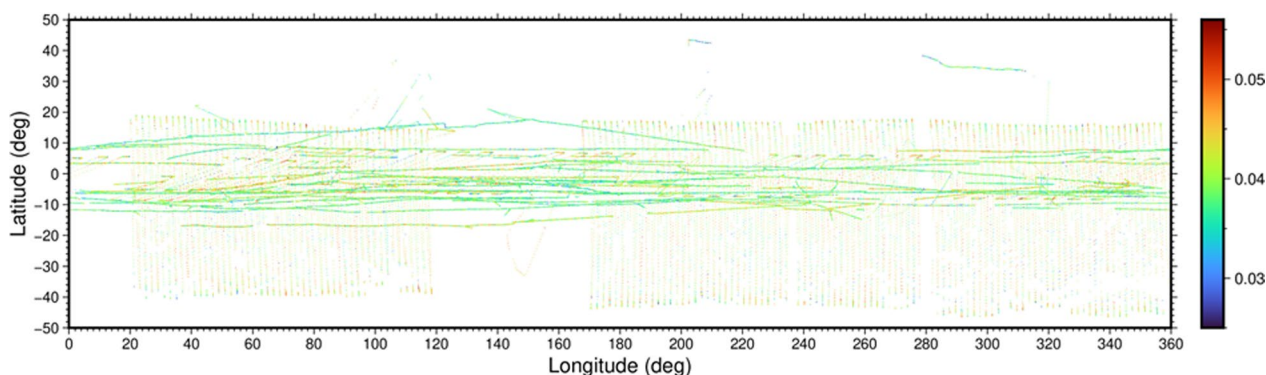
Yamada *et al. Earth, Planets and Space* (2022) 74:166

Page 13 of 18

Fig. 13 Map of 1.064 μm normal albedo for every footprint
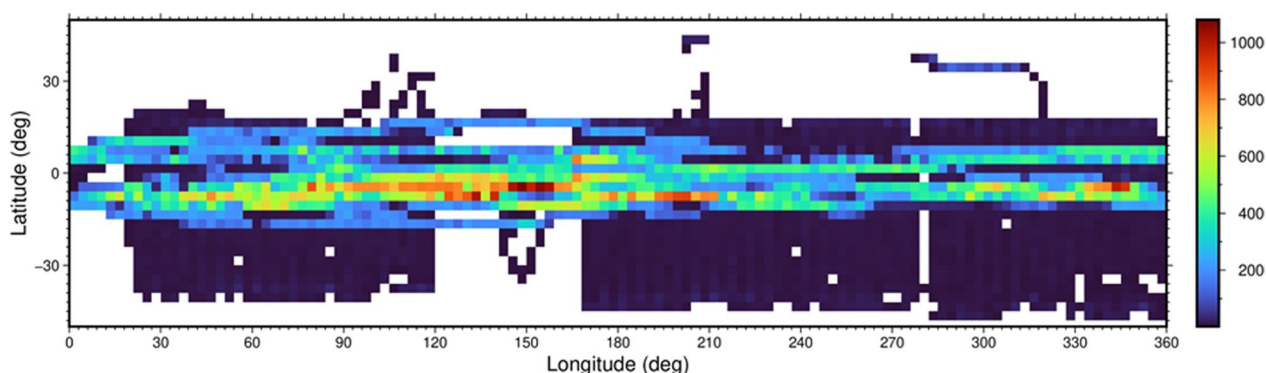

Fig. 14 Map of the number of footprints in each 3°-by-3° grid. Empty grids are shown in white color

situated around the equator, where observations are most frequently made. The average footprint number in each 3°-by-3° grid within ± 15° in latitude is 248, and that outside this band is 22. Furthermore, to secure statistical confidence, we eliminated the grids whose footprints were three or less. Then, the number of averaged grids is 2052.

As shown in Fig. 15a, the averaged grids were distributed between 40˚S and 20°N on Ryugu. The average and standard deviation are recalculated from the averages of every 3°-by-3° grid and are 0.0405 and 0.0027 (6.8% deviation). This standard deviation is lower than the 15.6% error for each laser shot in "Error of albedo derivation" section. Figure 15b also shows the standard deviations within each grid. Some grids include large boulders, resulting in large deviations, probably because their reflection is not reproduced well in the waveform simulation. This point is further discussed in the following chapter.

Figure 16 shows a histogram of the normal albedo. In addition, approximately 99% of the averaged grids have values between 0.03 and 0.05. The mode is 0.0425. The largest bin is between 0.040 and 0.045, including 54% of all counts.

Discussion

Normal albedo maps of Ryugu are also produced from Hayabusa2 ONC-T images (Yokota et al. 2021). The ONC-T has seven broadband filters ranging in wavelength from 0.3975 to 0.9451 μm (Tatsumi et al. 2020). The latter is closest to the wavelength of LIDAR. The global average of the normal albedo obtained by ONC-T at 0.9451 μm is 0.0399 ± 0.0005 (Yokota et al. 2021), which overlaps with our result of 0.0405 ± 0.0027 within 1 σ. Both Sugita et al. (2019) and Tatsumi et al. (2020) indicated flat spectral features in the visible range of ONC-T, and it appears that, this flatness continues until near-infrared wavelength around the equator.

Figures 15a and 16 show low and uniform albedo, paralleling the observations of ONC and NIRS3 of Hayabusa2 (Sugita et al. 2019; Kitazato et al. 2019). Furthermore, such albedo uniformity is comparable with that of C-type asteroid 253 Mathilde observed at 0.55 μm by NEAR Shoemaker (Clark et al. 1999). However, albedo maps derived from the Hayabusa2 mission have a higher resolution. In the OSIRIS-REx mission, another albedo map of the C-type asteroid Bennu was constructed using onboard camera images (Golish et al. 2021). Bennu's albedo distribution histogram has a median value

Yamada *et al. Earth, Planets and Space* (2022) 74:166
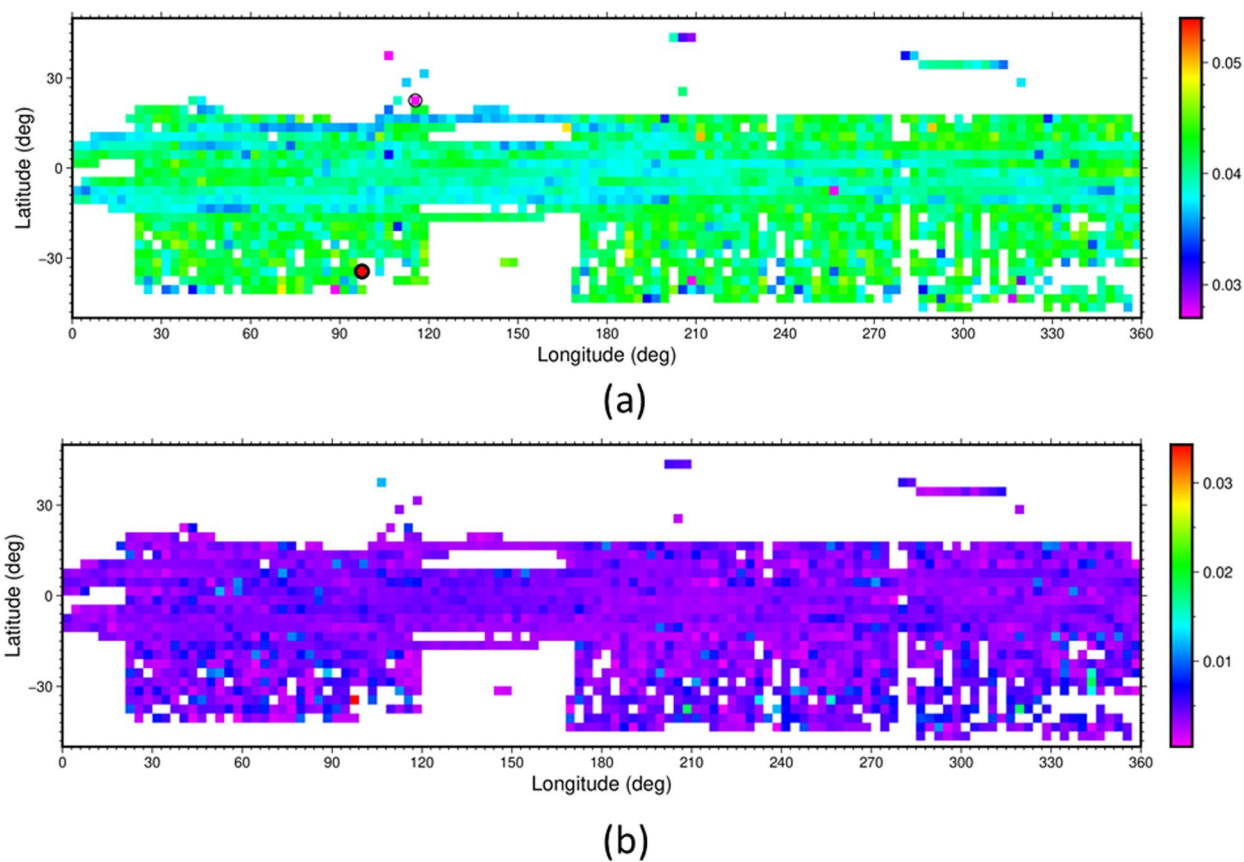
Page 14 of 18

(a)

(b)

Fig. 15 Gridded maps of **a** 1.064 μm normal albedos and **b** standard deviation in 3°-by-3° grids. The thick and thin circles in (**a**) indicate locations of the highest and lowest normal albedo grids, respectively
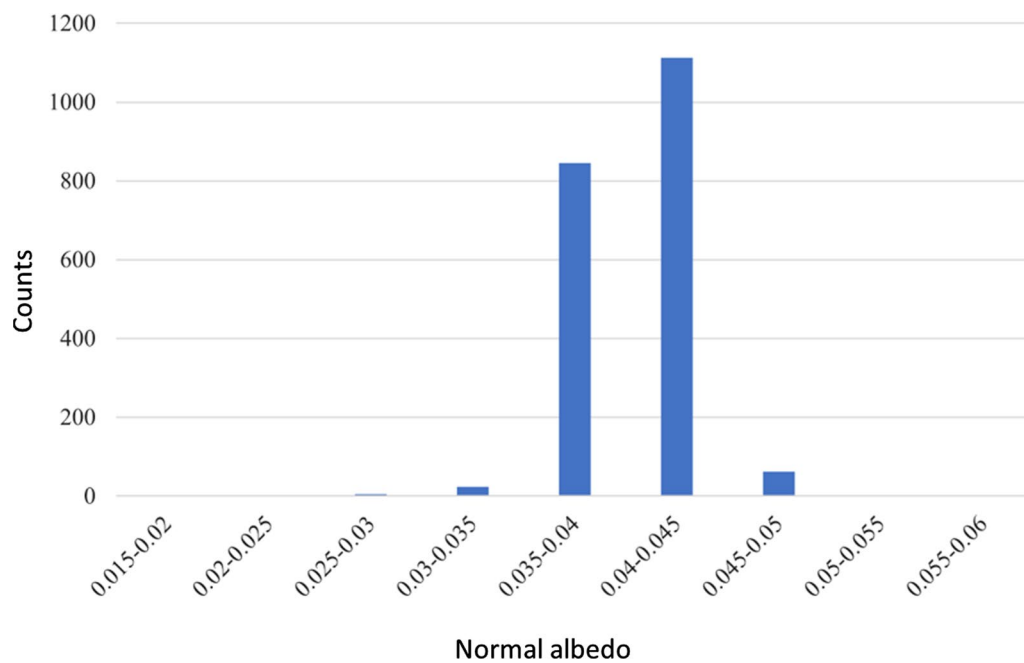

Fig. 16 Histogram of the normal albedo map shown in Fig. 15a

Yamada *et al. Earth, Planets and Space* (2022) 74:166

Page 15 of 18

Table 4 Anomalously high and low normal albedo grids

Grid number	Latitude	Longitude	Normal albedo	Standard deviation	Number of footprints	Average incident angle	Deviation of incident angle
1	− 43.5	316.5	0.0280	0.0036	7	46.3	0.21
2	− 40.5	88.5	0.0233	0.0088	9	44.3	1.76
3	− 37.5	208.5	0.0231	0.0183	4	32.6	9.23
4	− 37.5	319.5	0.0298	0.0181	4	44.8	2.49
5	− 34.5	97.5	0.0578	0.0343	7	42.3	10.5
6	− 7.5	256.5	0.0269	0.0068	28	44.2	12.9
7	10.5	211.5	0.0499	0.0038	7	38.6	3.55
8	13.5	166.5	0.0491	0.0021	7	35.1	3.36
9	13.5	289.5	0.0497	0.0044	5	43.3	3.71
10	22.5	115.5	0.0162	0.0086	8	39.6	5.2
11	37.5	106.5	0.0256	0.012	7	27.1	5.51
12	43.5	205.5	0.0306	0.0049	25	62.5	0.74
13	43.5	208.5	0.0293	0.0046	24	62.0	1.56

of 0.046 ± 0.002 in the visible range and is also similar to that of Ryugu. All remote sensing data, including our results, indicate a low albedo of C-type asteroids.

There are anomalous grids whose normal albedo deviates significantly from the global average. Table 4 lists four high albedo grids and nine low albedo grids. We set two criteria for Table 4 to exclude large deviations generated by chance. First, we chose the grids that included four or more footprints (Fig. 14). Second, we calculated the standard deviation of all 298,892 footprints, σ_{all}, and chose the grids whose average deviated more than $2\sigma_{\mathrm{all}}$ from the average of all grids. Although these two criteria are not unique, they guarantee that the probability that a grid is chosen by accident is less than 0.0068% under the assumption of normal distribution.

The highest normal albedo is 0.0578 at 35°S and 98°E (grid number 5 in Table 4). Ejima Saxum, an extraordinarily large (70 m in diameter) Type 1 boulder (Sugita et al. 2019), may influence such a high-normal albedo. This type of boulder is dark and possesses rugged surfaces and edges. The standard deviation in this grid (0.0343) is also the largest of all grids. The 0.9451 μm albedo in the Ejima Saxum region does not indicate such high values, but it is slightly darker than the average (Yokota et al. 2021). Waveform simulation of the returned pulses from this grid indicates that multiple reflections due to complex topography possibly result in a large albedo deviation.

The lowest normal albedo is 0.0163 ± 0.0086 (grid number 10 in Table 4) and is observed around 23°N and 116°E. This grid is located in the northern area of the Urashima crater, whose diameter of 290 m is the largest on Ryugu. However, this and other low-albedo grids in

Table 4 are not necessarily dark on the ONC-T albedo map (Yokota et al. 2021).

One possible cause of these high- and low-normal albedos is the shape model's insufficient resolution, which effectively decreases the slope. Our waveform simulation becomes incorrect if the laser shots hit the side of small boulders or steep slopes of a short-length scale. The Ryugu shape model also has an error in the horizontal direction (Noda et al. 2021). If there is a misalignment between the true location of the laser footprint and the estimation, it may result in albedo errors, especially in complicated surface terrain areas.

If the high- and low-normal albedos are real, they indicate an unusual property of the surface materials. The dark spots detected by LIDAR, but not by ONC, may indicate weak reflectance at 1.064 μm compared with that at visible wavelength. Nesvorny et al. (2005) described the reflectance of the C-complex decrease at near-infrared wavelengths due to space weathering. It is possible that the ONC missed these anomalous spots due to errors in the photometric correction. Furthermore, the reflectance at 1.064 μm could be an indicator of olivine and pyroxene. Detailed comparison and combination with the ONC image and other reflectance data will be important to reveal the causes of anomalous albedo spots.

Although the uncertainty is large, we also see small albedo variations between 0.03 and 0.05. Further investigation of global normal albedo variation may help us understand surface processes on Ryugu, because there remains unanalyzed data from Haybabusa2 LIDAR, which covers a broader area after the conjunction. Once the map is completed, comparisons with surface slope,

Yamada *et al. Earth, Planets and Space* (2022) 74:166

Page 16 of 18

roughness, and thermal inertia will be made to investigate the material properties of Ryugu.

Conclusion

We successfully observed laser intensities returned from the C-type asteroid Ryugu via the Hayabusa2 LIDAR. We established a method to retrieve normal albedo using the observed intensities and return pulse simulation. This is the first study to derive a normal albedo at 1.064 μm on Ryugu. Our analysis covers areas around the equator between about 40°S and 20°N. Each normal albedo is evaluated in a grid of 3°-by-3°. The global average and the error of normal albedo were determined as 0.0405 ± 0.0027 using 2052 grids with four or more footprints. Approximately half of the selected grids have albedo

values in the range of 0.04–0.045. This low and uniform albedo parallels the observations by ONC and NIRS3. This similarity suggests that our derivation method is useful for evaluating the normal albedo of a very rough surface using a laser altimeter. This new methodology, for example, can be applied if future middle- and small-class missions use a LIDAR as simple as the one onboard Hayabusa2. Our albedo map shows some anomalous spots. Further investigations using more LIDAR and ONC data will improve our understanding of the albedo variation of the C-type asteroid.

Appendix

See Table 5

Table 5 List of symbols

Symbol	Description	Note
Major parameters		
ρ	Normal albedo	Eqs. (2), (5)
i_{xy}	Incident angle of the laser at xy	Eq. (4)
α	Phase angle	Eq. (4)
E_{obs}	Energy received by the APD	Eq. (9)
D_R	Received pulse intensity	Eq. (9) "Experimental results" section
E_T	Energy injected into a laser footprint, *i.e.*, energy transmitted from LIDAR	Eq. (12)
D_T	Transmitted pulse intensity	Eq. (12)
β	Transmissivity of the optical system of the LIDAR receiver	Eq. (5)
φ_{eff}	Efficiency of the transfer from the surface to the aperture of the LIDAR telescope	Eq. (10)
ξ_{xy}	Law of reflection	Eq. (10)
ε_{xy}	Normalized beam pattern of the transmitted laser pulse in ds_{xy} shown in Fig. 1	"Waveform simulation using a shape model" section
$\tau(t)$	Normalized timewise intensity profile of the transmitted laser beam is shown in Fig. 2	
ds_{xy}	Area of the small element within a laser footprint on the Ryugu surface	
dt	Time interval of numerical integration	
c	Speed of light	
A_0	Aperture area of the FAR telescope	
L_{xy}	Distance between the LIDAR telescope and ds_{xy}	
Minor parameters		
G	Responsivity of the APD	Table 1
S_v	Integrated voltage of the input laser pulse recorded by the oscilloscope	Eq. (8)
S_v^{rec}	Integrated voltage of the 10-ns rectangular pulse recorded by the oscilloscope	Fig. 7
D_R^{rec}	Received pulse intensity of the 10-ns rectangular pulse	Eq. (7)
E_{obs}^{rec}	Energy input to the APD for 10-ns rectangular pulse	Eq. (6)
$R_S(D_R^{rec})$	Conversion function from rectangular pulse intensity to the output peak voltage of the APD	Eqs. (6), (7)
σ_{all}	Standard deviation of ρ for all 294,705 footprints	Chapter 6

Yamada *et al. Earth, Planets and Space* (2022) 74:166

Page 17 of 18

Abbreviations

APD	Avalanche photodiode
DU	Digital unit
EM	Engineering model
FOV	Field of view
GSE	Ground support equipment
LIDAR	Light detection and ranging
LOLA	Lunar orbiter laser altimeter
MLA	Mercury laser altimeter
NIRS3	Near-infrared spectrometer
OLA	OSIRIS-REx laser altimeter
ONC	Optical navigation camera
ONC-T	Optical navigation camera for telescopic nadir view
RMS	Root mean square
SPC	Stereo photo clinometry
S/N	Signal-to-noise ratio
TIR	Thermal infrared imager

Author contributions

RY led the coauthors in this original paper's data acquisition, analysis, and manuscript writing. KY coded waveform simulation and wrote related "Waveform simulation using a shape model" and "Errors of E_T and φ_{eff}" section. HA analyzed the parts of data in the LIDAR-EM experiment and supported the writing of "Estimation of E_{obs} from D_R" and Error of E_{obs} section. SO studied the albedo map and anomalous albedo spots and was a major contributor to writing Chapters 5 and 6. HS and HN supported the LIDAR-EM experiments and operations of the LIDAR during rendezvous with Ryugu. KM provided orbital information of the spacecraft, and NH disclosed the Ryugu shape model details. Asteroid science and characteristic of the C-type asteroid were written in cooperation with FY and SS. SA provided helpful information about the LIDAR of the former Hayabusa project. NN and TM are science and engineering PIs of the Hayabusa2 LIDAR. All the authors have read and approved the final manuscript.

Availability of data and materials

The data set of the Hayabusa2 LIDAR and related SPICE kernels used in this study are currently under review to be opened in Planetary Data System.

Declarations

Ethics approval and consent to participate
Not applicable.

Consent for publication
Not applicable.

Competing interests
This article does not relate with any competing interests.

Author details
[1]The University of Aizu, Ikki-Machi, Aizu-Wakamatsu, Tsuruga, Fukushima 965-8580, Japan. [2]National Astronomical Observatory of Japan, 2-21-1 Osawa, Mitaka, Tokyo 181-8588, Japan. [3]Institute of Space and Astronautical Science, Japan Aerospace Exploration Agency, 3-1-1 Yoshinodai, Chuo-Ku, Sagamihara, Kanagawa 252-5210, Japan. [4]Chiba Institute of Technology, 2-17-1 Tsudanuma, Narashino, Chiba 257-0016, Japan. [5]National Astronomical Observatory of Japan, 2-12 Hoshigaoka, Mizusawa-Ku, Oshu, Iwate 023-0861, Japan. [6]University of Occupational and Environmental Health, 1-1 Iseigaoka, Yahatanisi-Ku, Kitakyushu, Fukuoka 807-8555, Japan. [7]Nihon University, 7-24-1 Narashinodai, Funabashi, Chiba 274-8501, Japan. [8]Osaka University, 1-1 Machikaneyama, Toyonaka, Osaka 560-0043, Japan. [9]The Graduate University for Advanced Studies, SOKENDAI, Hayama, Kanagawa 240-0193, Japan.

References

Abe S, Mukai T, Hirata N et al (2006) Mass and local topography measurements of Itokawa by Hayabusa. Science 312:1344–1347

Barnouin OS, Daly MG, Palmer EF et al (2020) Digital terrain mapping by the OSIRIS-REx mission. Planet Space Sci 180(104764):1–16

Binzel RP, Morbidelli A, Merouane S, DeMeo FE, Birlan M, Vernazza P, Thomas CA, Rivkin AS, Bus SJ, Tokunaga AT (2010) Earth encounters as the origin of fresh surfaces on near-Earth asteroid. Nature 463:331–334

Bus SJ, Binzel RP (2002) Phase II of the small main-belt asteroid spectroscopic survey: a feature-based taxonomy. Icarus 158(1):146–177

Clark BE, Veverka J, Helfenstein P, Thomas PC, Bell JFIII, Harch A, Robinson MS, Murchie SL, McFadden LA, Chapman CR (1999) Near photometry of asteroid 253 Mathilde. Icarus 140:53–65

Daly MG, Barnouin OS, Dickinson C et al (2017) The OSIRIS-REx laser altimeter (OLA) investigation and instruments. Space Sci Rev 212:899–924

Daly MG, Barnouin OS, Seabrook JA et al (2020) Hemispherical differences in the shape and topography of asteroid (101955) Bennu. Sci Adv 6:41. https://doi.org/10.1186/s40623-014-0158-y

Golish DR, Shultz NK, Becker TL et al (2021) A high-resolution normal albedo map of asteroid (101955) Bennu. Icarus 355(114133):1–18

Jantunen H, Raitala J (1983) A simple method for planetary surface ruggedness estimation. Moon Planets 29:7–13

Kitazato K, Clark BE, Abe M, Abe S, Takagi Y, Hiroi T, Barnouin-Jha OS, Abell PA, Lederer SM, Vilas F (2008) Near-infrared spectrophotometry of asteroid 25143 Itokawa from NIRS on the Hayabusa spacecraft. Icarus 194:137–145

Kitazato K, Milliken RE, Iwata T et al (2019) The surface composition of asteroid 162173 Ryugu from Hayabusa2 near-infrared spectroscopy. Science 364:272–275

Le Corre L, Sanchez JA, Reddy V, Takir D, Cloutis EA, Thirouin A, Becker KJ, Li J, Sugita S, Tatsumi E (2018) Ground-based characterization of Hayabusa2 mission target asteroid 162173 Ryugu: constraining mineralogical composition in preparation for spacecraft operations. Monthly Not Roy Astron Soc 475(1):614–623

Li J-Y, Helfenstein P, Buratti BJ, Takir D, Clark BE (2015) Asteroid photometry. In: Michel P et al (eds) Asteroid IV. University of Arizona Press, Tucson

Matsumoto K, Noda H, Ishihara Y et al (2020) Improving Haysabu2 trajectory by combining LIDAR data and a shape model. Icarus 338:113574

Mizuno T, Kase T, Shiina T, Mita M, Namiki N, Senshu H, Yamada R, Noda H, Kunimori H, Hirata N, Terui F, Mimasu Y (2017) Development of the laser altimeter (LIDAR) for Hayabusa2. Space Sci Rev 208:33–34

Mukai T, Abe S, Hirata N et al (2007) An overview of the LIDAR observations of asteroid 25143 Itokawa. Adv Space Res 40:187–192

Nesvorny D, Jedicke R, Whiteley RJ, Ivezic Z (2005) Evidence for asteroid space weathering from the Sloan Digital Sky Survey. Icarus 173:132–152

Neumann GA, Cavanaugh JF, Sun X, Mazarico E, Smith DE, Zuber MT, Mao D, Paige DA, Solomon SC, Ernst CM, Barnouin OS (2013) Bright and dark polar deposits on Mercury: evidence for surface volatiles. Science 339:296–300

Neumann GA, Barker MK, Mazarico E, Daly MG, Barnouin OS, Jawin ER, Lauretta DS (2020) Global and local variations in 1064 nm normal albedo of Bennu from the OSIRIS-REx laser altimeter. In: 51st Annual Lunar and Planetary Science Conference, Cancellation

Noda H, Senshu H, Matsumoto K et al (2021) Alignment determination of the Hayabusa2 laser altimeter (LIDAR). Earth Planets Space 73:21. https://doi.org/10.1186/s40623-020-01342-8

Oren M, Nayar SK (1994) Generalization of Lambert's reflectance model. In: Proceeding of the 21st annual conference on computer graphics and interactive techniques. pp. 239–246

Reddy V, Nathues A, Corre L et al (2012) Color and albedo heterogeneity of Vesta from Dawn. Science 336:700–703

Yamada *et al. Earth, Planets and Space* (2022) 74:166

Page 18 of 18

Seabrook JA, Daly MG, Barnouin OS, Johnson CL, Nair AH, Bierhaus EB, Boynton W, Espiritu RC, Gaskell RW, Palmer E, Nguyen L, Nolan M, Lauretta DS (2019) Global shape modeling using the OSIRIS-Rex scanning laser altimeter. Planet Space Sci 177:104588. https://doi.org/10.1016/j.pss.2019.07.003

Senshu H, Oshigami S, Kobayashi M, Yamada R, Namiki N, Noda H, Ishihara Y, Mizuno T (2017) Dust detection mode of the Haybusa2 LIDAR. Space Sci Rev 208:65–79

Shkuratov Y, Kaydash V, Korokhin V, Velikodsky Y, Opanasenko N, Videen G (2011) Optical measurements of the Moon as a tool to study its surface. Planet Space Sci 59:1326–1371

Smith DE, Zuber MT, Jackson GB et al (2010) The lunar orbiter laser altimeter investigation on the lunar reconnaissance orbiter mission. Space Sci Rev 150:209–241

Sugita S, Honda R, Morota T et al (2019) The geomorphology, color, and thermal properties of Ryugu: implications for parent-body processes. Science 364(eaaw0422):1–11

Sugita S, Kuroda D, Kameda S, Hasegawa S, Kamata S, Abe M, Ishiguro M, Takao N, Yoshikawa M (2013) Visible spectroscopic observation of asteroid 162173 (1999ju3) with the Gemini-s telescope. In: Abstract of 44th DPS Meeting. American Astronomical Society, Reno, Nevada 14–19 October 2012

Sun X, Neumann GA (2015) Calibration of the Mercury Laser Altimeter on the MESSENGER spacecraft. IEEE Trans Geosci Remote Sens 53(5):2860–2874

Tatsumi E, Domingue D, Schröder S et al (2020) Global photometric properties of (162173) Ryugu. Astron Astrophys 639:A83

Tatsumi E, Sugimoto C, Rui L et al (2021) Collisional history of Ryugu's parent body from bright surface boulders. Nat Astron 5:39–45

Vilas F (2008) Spectral characteristics of Hayabusa2 near-Earth asteroid targets 162171 1999JU3 and 2001 QC34. Astron J 135:1101–1105

Watanabe S, Hirabayashi M, Hirata N et al (2019) Hayabusa2 arrives at the carbonaceous asteroid 162173 Ryugu – a spinning top-shaped rubble pulse. Science 364(6437):268–272

Yamada R, Senshu H, Namiki N, Mizuno T, Abe S, Yoshida F, Noda H, Hirata N, Oshigami S, Araki H, Ishihara Y, Matsumoto K (2017) Albedo observation by Hayabusa2 LIDAR: instrument performance and error evaluation. Space Sci Rev 208:49–64

Yamamoto K, Otsubo T, Matsumoto K et al (2020) Dynamic precise orbit determination of Hayabusa2 using laser altimeter (LIDAR) and image tracking data sets. Earth Planets Space. https://doi.org/10.1186/s40623-020-01213-2

Yokota Y, Honda R, Tatsumi E et al (2021) Opposition observation of 162173 Ryugu: normal albedo map highlights variations in regolith characteristics. Planet Sci J 2(177):1–32

Yokota Y, Honda R, Domingue D et al. (2022) Regional photometry of asteroid Ryugu with multiple photometric models. In: Abstract of 53rd Lunar Planet. Science Conference, The Woodlands, Texas, 7–11 March, 2022

Zuber MT, Head JW, Smith DE, Neumann GA, Mazarico E, Torrence MH, Aharonson O, Tye AR, Fassett C, Rosenburg MA, Melosh HJ (2012) Constraints on the volatile distribution within Shackleton crater at the lunar south pole. Nature 486:378–382

Publisher's Note